On the daytime micro-climatic conditions inside an idealized 2D urban canyon

Schrijvers, P. J.C.; Jonker, H. J.J.; de Roode, S. R.; Kenjereš, S.

DOI
10.1016/j.buildenv.2019.106427

Publication date
2020

Document Version
Final published version

Published in
Building and Environment

Building and Environment 167 (2020) 106427

Contents lists available at ScienceDirect

Building and Environment

journal homepage: http://www.elsevier.com/locate/buildenv

On the daytime micro-climatic conditions inside an idealized 2D urban canyon

P.J.C. Schrijvers [a,*], H.J.J. Jonker [a], S.R. de Roode [a], S. Kenjereš [b]

[a] Faculty of Civil Engineering and Geotechnology, Delft University of Technology, Stevinweg 1, 2628CN, Delft, the Netherlands
[b] Faculty of Applied Sciences, Delft University of Technology, Van der Maasweg 9, 2629HZ, the Netherlands

ARTICLE INFO

Keywords:
urban heat island
Mean radiant temperature
Urban comfort
Surface energy balance
Computational fluid dynamics

ABSTRACT

This study investigated the surface temperature, air temperature and mean radiant temperature inside an idealized 2D street geometry during daytime. The goal was to unravel the relative impact of radiative transfer, heat conduction and ventilation to the urban heat budget. A building-resolving simulation model has been used, which represents these processes at a 1 m spatial resolution. Different combinations of the canyon height to width ratio (H/W) and physical mechanisms were investigated. Shortwave radiation is the main source of energy, and for small H/W can be higher at the canyon ground level compared to flat terrain due to multiple reflections. The longwave trapping effect has the second largest contribution and becomes relatively more important with increasing H/W ratio. The influence of the interior building temperature is small. Surface temperature and mean radiant temperature are closely related, since both are largely controlled by radiative properties. No straightforward relation was found between surface temperature and air temperature, since air temperature is dependent on the competing mechanisms of forced and natural convection. A small increase in air temperature inside the canyon was observed compared to the ambient temperature above roof level. The inclusion of all key physical processes in high detail resulted in large computational requirements. If multiple reflections by the building facades are small, the more traditional, yet much simpler view factor approach will strongly reduce the computational costs as compared to the Monte Carlo technique. The influence of using the view factors on the results must be investigated.

1. Introduction

During clear nights with weak winds, cities tend to be 1–10 °C warmer than the surrounding rural environment at night. This phenomenon has been observed for both small and large cities, in the tropics as well as in colder regions, and is called the Urban Heat Island (UHI) effect [1–5]. However, the daytime UHI effect is much smaller [2,6] and can even be negative, even in cold climates [7]. Furthermore, the daytime and night time UHI can have different distribution patterns and intensities over relatively short distances of less than 1 km, as was found from measurements by Soltani and Sharifi [8]. This also holds for surface temperatures and mean radiant temperature, which is a quantity indicative of the human thermal comfort. The mean radiant temperature only depends on radiation, and is used in the computation of apparent temperatures like the Physiological Equivalent Temperature (PET, Höppe [9]) and the Universal Temperature Climate Index (UTCI, Fiala et al. [10]). Because of the higher temperatures, radiation, and thus heat load, human comfort in the city is more critical during daytime as compared to the night.

Klysik and Fortuniak [2] studied the daytime atmospheric UHI effect of the town Lodz in Poland by using fixed point measurements from a weather station in the city centre over two different periods of three years. They found that on days with clear skies, there are large thermal contrasts within the city. In areas with narrow streets, the air close to the ground may be cooler than the rural environment due to shading of the ground surface. Klysik and Fortuniak [2] state that the radiation and energy budget of roofs play an important role in that scenario. A warm layer of air can be formed at roof level, while the air inside the canyon remains cool due to the shading effect, creating a local inversion layer between canyon and roof level and limiting the vertical exchange of air in the street canyons.

In addition to air temperature, mean radiant temperature is also measured in dedicated field campaigns. Such measurements were conducted (amongst others) by Lindberg et al. [11], who observed large

* Corresponding author.
E-mail address: p.j.c.schrijvers@tudelft.nl (P.J.C. Schrijvers).

https://doi.org/10.1016/j.buildenv.2019.106427
Received 3 July 2019; Received in revised form 8 September 2019; Accepted 23 September 2019
Available online 26 September 2019

local variations of mean radiant temperature. On a large open square in the city centre of Göteborg in Sweden, a peak value in mean radiant temperature of 57 °C was found, which is on the threshold for moderate heat stress [12,13]. In contrast, simultaneous measurements in a courtyard resulted in a mean radiant temperature of 17 °C when shaded, which quickly raised to 27 °C when the measurement location was directly sunlit. These measured values are well below the threshold of moderate heat stress of 55 °C, indicating the large impact of geometric properties and shading.

Even though the mean radiant temperature can be measured and the atmospheric UHI frequently observed, the urban UHI is a difficult phenomenon to interpret, due to its spatial inhomogeneity. When interpreting profiles of thermodynamic variables from a single measurement location, the effect of advection across the heterogeneous urban surface should also be taken into account, which is difficult to observe or quantify [14]. To overcome the local nature of measurements, numerical models can be used to study the urban environment, in which the complexity and non-linearity of the urban environment can be studied in a systematic manner. Often, these models apply on a larger scale (meso-scale) and the urban street canyon is parametrized. For instance, a meso-scale model (Weather and Research Forecasting model, WRF) coupled with a single-layer urban canopy model (SLUCM, [15]), was used by Ryu and Baik [7]. The building height ($H = 15$ m) over street width ($W = 15$ m) ratio (H/W) used was $H/W = 1.0$. Their study indicated that during daytime the impervious surfaces (including the reduction in surface moisture availability and increased thermal inertia) contribute most to the urban heat island (+2.1 °C). The 3D urban geometry (transfer of energy in vertical walls, shading, radiative trapping and reduction in ventilation) actually cools the city (−0.5 °C).

Ryu and Baik [7] used just a single H/W ratio, though it is known that this parameter has a large impact on the UHI effect [16]. Marciotto et al. [17] investigated the influence of the aspect ratio and mean building height on local canopy energy fluxes by using an Urban Canopy Model (UCM) similar to Masson [18]. A north-south oriented canyon was used, and a full daily cycle was investigated. Results for one time-instance at midday (12:00) were discussed. Increasing the H/W ratio from 0.5 to 10.0, decreases the net radiation, as well as the sensible heat flux, by an amount of 120 Wm^{-2} (from 490 to 370) and 300 Wm^{-2} (from 360 to 60), respectively. The reduction in absorbed energy is compensated by the conductive heat flux, which transports energy towards the surface, and increases by 180 Wm^{-2}.

Theeuwes et al. [19] differentiated the two compensating radiative effects in the urban canyon: shadow casting and longwave trapping. The net effect depends on the amount of available shortwave radiation penetrating the canyon. It was found that for $H/W = 1.0$ the largest UHI effect is present. With increasing H/W ratio shading effects start to dominate over the longwave trapping effect during the day, and the UHI is decreasing.

All previously mentioned numerical studies used a meso-scale model in which the urban environment is parametrized. Therefore, results were obtained for the canyon as a whole, or for individual surfaces. When more spatial details are desired, smaller scale models are available that focus on the urban micro-scale. These include for instance Solweig [11], RayMan [20], TUF-3D [21] and envi-MET [22]. Hertel and Schlink [23] developed a method for decomposing the urban heat island intensity at the neighbourhood scale. Envi-MET simulations are used as input, after which the surface energy balance is translated into temperature differences between two neighbourhoods. Unfortunately, no results were presented of a case study, nor validation of the model. In addition to the above models, generic Computational Fluid Dynamics (CFD) models are often applied in which surface temperature is prescribed and air flow is investigated. Toparlar et al. [24] have performed an extensive review of CFD studies on the urban micro climate. They conclude that at present CFD modelling results can be often validated from observations, and CFD models are being increasingly applied for realistic case studies, including the assessment of the effect of adaptation measures. One specific example is Robitu et al. [25], who used a coupled CFD, radiation and conduction model to investigate the effect of vegetation and ponds on the urban micro-climatic conditions. The presence of water ponds and trees improves the urban thermal comfort in summer during day time by cooling the air and shading the urban surface. The influence of trees and ponds was not distinguished, nor the influence of trees and ponds on the different components of the surface energy balance.

Within the current study and [26], a new numerical model (called URBSIM) has been developed, which computes all processes at a 1 m spatial resolution at the canyon surface. The goal of the present study was to identify the mechanisms that control daytime surface temperature, air temperature and mean radiant temperature within a single canyon at a high resolution. As shown in the literature review, these processes are currently known for the canyon as a whole, thereby neglecting the spatial variability over a single surface. The processes taken into account are shortwave radiation, longwave radiation, conduction and turbulent transport of heat. Our objective was three-fold: 1) disentangle the mechanisms involved in the urban heat budget, 2) quantify the relation between surface temperature, air temperature and mean radiant temperature within a single street canyon, and 3) create insight for future studies into which processes can be parametrized at the urban micro-scale. The focus in this study was on the different processes and interactions, not so much on the most accurate representation of the actual urban geometry. This was also reflected in our assumption of an idealized 2D geometry.

2. Methods and case set-up

The 2D micro-scale model URBSIM, that was discussed in Schrijvers et al. [26,27] has been used. URBSIM couples a Monte-Carlo radiation model, 1D heat conduction equation for the conductive heat flux into buildings and the ground and a Computational Fluid Dynamics (CFD) model for the convective heat fluxes. In the present study, the 2D micro-scale model was extended with a new boundary condition for the interior building temperature, and mean radiant temperature can be routinely computed at any time and at any location. A 2D version of the model was used in order to simplify the geometrical complexity. A similar case set-up is used as in Ref. [26], and a range of H/W ratios were considered (0.0, 0.5, 1.0, 2.0). In addition to different canyon aspect ratios, also the inclusion of different physical processes wereconsidered. Starting from a radiation only case, complexity was added by including the conductive heat flux and sensible heat flux. The canyon orientation is north-south, such that building facades are east-facing or west-facing. This is a typical orientation for 2D studies, and was also used in Schrijvers et al. [26]. A spatial resolution of 1 m was used at the building surface, and although a full diurnal cycle was modelled, here we only report the situation for a solar zenith angle of 28.9° which corresponds to solar noon for the Netherlands at June 21. Details of the model and validation are discussed in Schrijvers et al. [26], and only a brief description will be given here for convenience. Extensions of the model for this study are discussed in more detail.

2.1. Radiative transfer

Radiative transfer is computed by the Monte-Carlo model that was developed in Schrijvers et al. [26], in which photon paths are computed for four radiative components: 1) diffuse shortwave radiation from the sky, SW_{dif}, 2) direct shortwave radiation from the sky, SW_{dir}, 3) longwave radiation emitted by the sky, LW_{sky} and 4) longwave radiation emitted by the surface, LW_{out} computed as:

$$LW_{out} = \sigma \varepsilon_s T_s^4 \quad (1)$$

with σ the Stefan-Boltzmann constant in [$Wm^{-2}K^{-4}$], ε_s the emissivity of the surface and T_s the surface temperature in each grid cell in [K].

Note that reflection-events are not addressed separately; a photon emitted as direct radiation will be labelled SW_{dir} after a scattering event at the surface. The only exception is LW_{trap}, which is LW_{out} that is absorbed at another surface. Due to the 2D assumption, the azimuthal angle is not taken into account and only the solar-zenith angle is used to describe the solar position. This means that the solar position is only described in the east-west plane, and that the north-south plane is discarded. The azimuthal angle is only taken into account in the computation of the amount of incoming solar radiation at the top of the domain.

The photon packets trajectory is computed from cell face to cell face until a surface is hit. A fraction of the energy $(1-\zeta)$ is absorbed at the surface, which is related to the albedo of the surface (shortwave radiation) and emissivity (longwave radiation). Note that radiation does not interact with the air inside the canyon, but only interacts at the surface.

The magnitude of the shortwave radiative flux is based on a parametrization proposed by Skartveit et al. [28] and assuming clear skies. Maximum values for downwelling shortwave radiation and the constant value for LW_{sky} that are used at roof level, are shown in Table 1. Although LW_{sky} has a diurnal variation in reality, this is not taken into account in the current study. Similarly, a constant value is used for inlet air temperature and wind speed. Kirchoff's law is assumed for broadband radiation, indicating that the same value is used for absorption (LW_{sky}) and emission (LW_{out}) of longwave radiation at the surface ($\alpha = \varepsilon$).

2.2. Mean radiant temperature (T_{mrt})

The existing model has been extended to diagnose the mean radiant temperature, which is computed by

$$T_{mrt} = \sqrt[4]{\frac{S_{str}}{\varepsilon_p \sigma}} \tag{2}$$

where S_{str} is the local mean radiant flux density [Wm^{-2}] and ε_p the emissivity of the human skin, which is a constant independent of the application with a value of 0.97.

The mean radiant flux density can be regarded as the amount of radiation (both shortwave and longwave) that is absorbed by a person. It is computed following Thorsson et al. [29].

Table 1
Input constants for radiation, heat conduction into the urban material and the CFD model.

Radiation	
Emissivity ε	0.95
Albedo α	0.40
Latitude	52° 22′ N
Longitude	4° 53′ E
Start day	2012-06-10 00:00
End day	2012-06-18 23:59
max SW_{dir}	833.1 Wm^{-2}
max SW_{diff}	84.2 Wm^{-2}
	325 Wm^{-2}
	Heat conduction
λ	0.72 $Wm^{-1}K^{-1}$
ρ	1920 kgm^{-3}
	835 $Jkg^{-1}K^{-1}$
	Computational Fluid Dynamics
	20 °C
U	4.0 ms^{-1}
cell width	1.0 m

$$S_{str} = (1-\alpha_k)\sum_{n=1}^{6} SW_n F_n + \varepsilon_p \sum_{n=1}^{6} LW_n F_n \tag{3}$$

where n is the orientation (north, east, south, west, top, bottom), α_p is the albedo of the human body (with a standard value of 0.3), SW_n the total shortwave radiative flux in [Wm^{-2}], LW_n the total longwave radiative flux in [Wm^{-2}] and F_n a geometric factor representing a standing human body. A summation is performed over the 4 cardinal points (north, east, south, west), for which the geometric factor is set to 0.22 for each direction, while the geometric factor is set to 0.06 for radiation entering from the top and bottom [11]. Since a 2D setting is used in this study, information is missing on the two faces that are occupying the sides of the canyon. These missing radiative fluxes are taken as the average of the two cardinal points that are available. This can physically be seen as computing mean radiant temperature on a square surrounded by obstacles.

2.3. Mean radiant temperature validation

The computation of T_{mrt} within the Monte-Carlo model is validated against values of the actinic flux from Madronich [30]. In that paper, a derivation of the actinic flux (also called integrated density or flux density) is given and solutions are presented for the irradiance for direct and diffuse shortwave radiation.

Two cases are considered. In the first case direct radiation of 800 Wm^{-2} has been emitted with a solar zenith angle of 0° onto a diffuse scattering surface with albedo $\alpha = 1$ (no absorption). For this configuration, the horizontal flux should be half of the incoming energy (400 Wm^{-2}). The left panel of Fig. 1 shows the horizontal and vertical flux directions, which show that the horizontal component is 400 Wm^{-2} (50%) of the incoming direct radiation. There are small spatial differences due to the Monte-Carlo method, which are around 2 Wm^{-2}. The averaged difference is 0.8 Wm^{-2} for the vertical components (0.1%) and 0.15% for the horizontal components. These differences decrease with increasing number of photons.

In the second simulation setup, diffuse radiation (100 Wm^{-2}) is emitted, for which [30] derived that the irradiance is equal in all directions (this only holds for a perfect reflecting surface, with $\alpha = 1$). Results are shown in the right panel of Fig. 1, which shows an uniform distribution of 100 Wm^{-2} with fluctuations of 0.5 Wm^{-2}.

The Monte-Carlo radiation model performs well against the results by Ref. [30], and as such will be used in the remainder of this study. The spatially averaged Monte-Carlo results are within 0.15% of Madronich [30].

2.4. Conductive heat flux

The conductive heat transfer is computed using the temperature gradient inside the urban material (building walls and layers beneath the street)

$$G_i = -\lambda \frac{\partial T}{\partial x_i} \tag{4}$$

where λ is the thermal conductivity of the material in [$Wm^{-1}K^{-1}$] (see Table 1) and x_i the distance into the ground or building surface in [m]. The value of λ used in this study is that of brick, which is close to the thermal conductivity of asphalt and medium to dense concrete. Note that this is a highly simplified representation of the building walls, in which normally two layers of brick are used with a cavity in between. To simplify the problem, the cavity is not taken into account. Furthermore, no sensitivity study on other building materials is conducted, which is left for future work. The temperature profile is computed using the 1D heat conduction equation

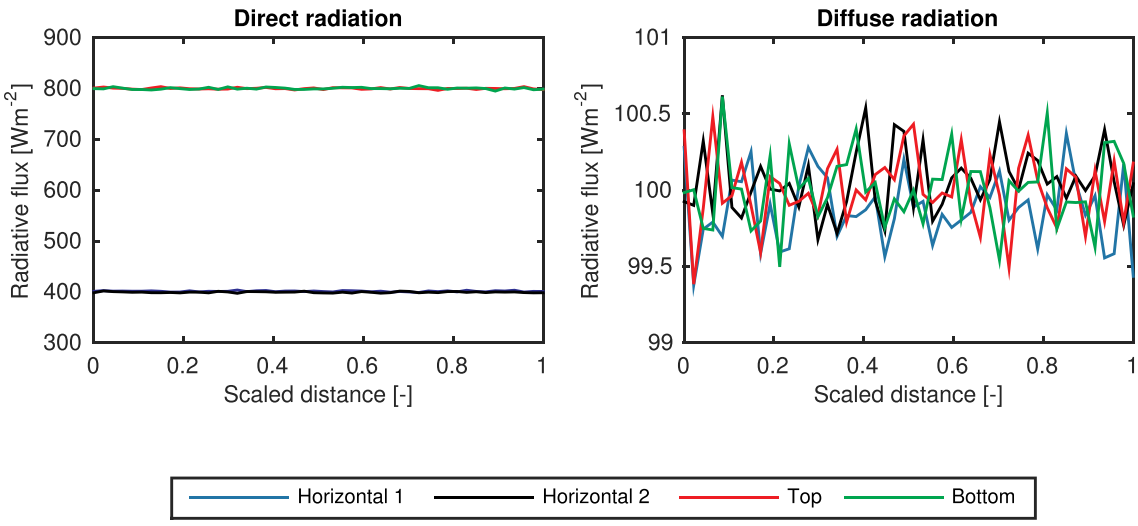

Figure 1. Validation of radiative fluxes for two numerical tetsts against analytical results by Madronich [30]. Results show the horizontal flux (eastward and westward) for direct shortwave flux density for all directions and diffuse shortwave flux density for all direction. Input for the direct shortwave radiation is 800 Wm^{-2} and 100 Wm^{-2} for the diffuse shortwave radiation.

$$\frac{\partial T}{\partial t} = k_d \frac{\partial^2 T}{\partial x_i^2} \tag{5}$$

where k_d is the thermal diffusivity in [m^2s], based on the conductivity λ, density ρ in [kgm^{-3}] and specific heat C_v of the ground or obstacle in [$Jkg^{-1}K^{-1}$].

$$k_d = \frac{\lambda}{\rho C_v} \tag{6}$$

Two different boundary conditions are used for the building interior. The first is a zero flux boundary condition at a distance of 1 m into the ground or 0.25 m into an obstacle. It was found that diurnal temperature cycle does not influence the interior temperature in the ground over more than 1 m, which is why this distance was used. The distance of 0.25 m for the fixed building temperature is based on the typical thickness of a building wall. Alternatively, a fixed interior temperature is used of 20 °C at the same distance into the ground and obstacle. The choice of 20 °C is based on a temperature inside a building that is comfortable. As a consequence of the zero-flux boundary condition, the interior building temperature follows from the absorbed radiation, sensible heat flux and conductive heat flux of previous time steps. With a constant, prescribed interior temperature, the energy inside the building is dissipated or generated, which can act as an unlimited source of energy. Physically, this can be seen as using an extremely efficient air-conditioning unit which is able to maintain the prescribed interior temperature. A time step of the global model is used of 6 min, except for the conductive heat flux where a time step of 1 s is used. The surface temperature of each grid cell is thus updated every 6 min. This will be discussed in more detail in section 2.7.

2.5. Computational Fluid Dynamics (CFD) model

Ventilation effects are computed by an in-house developed CFD model [31–35]. This model uses the Transient Reynolds-Averaged Navier-Stokes (T-RANS) equation to solve the wind field and air temperature distribution, and includes buoyancy effects.

The unknown Reynolds stresses $\overline{u_i u_j}$ [m^2s^{-2}] are computed using the $k-\varepsilon$ turbulence model, which relates the turbulent stresses to the turbulent kinetic energy k [m^2s^{-2}] and dissipation ε [m^2s^{-3}]. The model coefficients (C_μ, σ_k, σ_ε, $C_{\varepsilon 1}$, $C_{\varepsilon 2}$ and $C_{\varepsilon 3}$, see Table 2) used are taken from the standard k-ε model, as often used for a wide range of turbulent flows in street canyons ([36–38]).

Table 2
Model coefficients used in the standard $k-\varepsilon$ turbulence model.

C_μ	σ_k	σ_ε	$C_{\varepsilon 1}$	$C_{\varepsilon 2}$	$C_{\varepsilon 3}$
0.09	1.0	1.3	1.44	1.92	1.44

In addition to the velocity field, the temperature field is solved by using the T-RANS equations. The unknown turbulent heat flux $\overline{\theta u_i}$ [$ms^{-1}K$] is computed using the Simple Gradient Diffusion Hypothesis, where the turbulent flux is related to the temperature gradient and the turbulent viscosity

$$-\overline{\theta u_i} = \frac{\nu_t}{Pr_t}\frac{\partial T}{\partial x_i}. \tag{7}$$

with ν_t the eddy viscosity [m^2s^{-1}], and Pr_t the turbulent Prandtl number (the ratio between the eddy diffusivity for momentum and heat transfer K_m/K_h), and is set to 0.86. Although the value of the turbulent Prandtl number depends on stability [39,40], we set Pr_t to 0.86 which is typically used in commercial CFD codes and is also in between the range between 1/3 and 1 commonly used in large-eddy simulation models for convective and stable conditions [41].

The sensible heat flux at each individual surface grid cell is defined as

$$SHF_i = \rho c_p \overline{\theta u_i} \tag{8}$$

where ρ is the density of air (1.208 kgm^{-3}) and c_p the specific heat capacity of air (1004 $Jkg^{-1}K^{-1}$). The sensible heat flux is computed based on the temperature gradient between surface and air in the neighbouring grid cell. The Boussinesq approximation is used, stating that density differences can be neglected except for the buoyancy term. Buoyancy effects are taken into account in the computation of the temperature field, and are therefore not specifically required in the computation of the sensible heat flux.

2.6. Integrated energy balance model

All sub-models compute a part of the total surface energy balance, which dictates that all fluxes should balance:

$$SW_{dir} + SW_{dif} + LW_{sky} + LW_{trap} = LW_{out} + SHF + G \tag{9}$$

where *SHF* is the sensible heat flux (for *SHF* >0 there is heating of air) and *G* the conductive heat flux (for *G* >0 energy is added to the ground). The latent heat flux (evaporation of water) is not taken into account in this study. Multiple reflections of radiation are not addressed separately, but are included in the terms of SW_{dir}, SW_{dif} and LW_{sky}.

The controlling parameter for the surface fluxes is the surface temperature. A skin layer is assumed to prevent large variations in surface temperature in time

$$\Delta_{skin}\rho_{skin}C_{v,skin}\frac{\partial T_s}{\partial t}=\Gamma \tag{10}$$

with Γ the flux imbalance resulting from the surface energy balance and $\Delta_{skin}\rho_{skin}C_{v,skin}=0.01$ $JK^{-1}m^{-2}$, which results from a very thin layer Δ_{skin}. This also creates an under-relaxation-factor, which helps to stabilize the simulation.

For a time step, all fluxes in the surface energy balance are computed based on the surface temperature of the previous time step in each building surface grid cell. This can result in a small flux imbalance Γ. Based on the flux imbalance and old surface temperature, the surface temperature for the new time step is computed. Surface temperature is thus not a fixed value, but interactive through all surface fluxes.

The time step of 6 min is used for the Monte-Carlo radiation model, CFD model and integrated model, while the conductive heat flux model uses a time step of 1 s. The time step of 6 min is based on the movement of the shadow: for the cases considered here, the shadow does not travel more than 1 grid cell per time step. Ideally, a smaller time step would be used for the CFD model, but this would increase computation times significantly.

2.7. Test cases and methodology

To study the effect of different physical processes as a function of the H/W ratio, an idealized 2D urban geometry has been used consisting of 10 obstacles which are spaced $W=50$ m apart. By using an array of obstacles, a fully developed flow pattern is found in the most downwind street canyons, which indicates that more obstacles would not change the flow in the next canyon. The establishment of a fully developed flow after multiple obstacles has been obtained from a sensitivity analysis, and is confirmed by literature [38,42]. A uniform grid of 1 m is used. From sensitivity studies, it was found that for a convergence of the modelling results, a canyon should be covered by at least 20 x 20 cells to be grid independent. The total number of cells ranges between 400,000 (for $H/W=0.5$ up to 1,500,000 for $H/W=2.0$. All buildings are $B=25$ m wide, while building height is varied between 0 m (H/W=0.0), 25 m (H/W=0.5), 50 m (H/W=1.0) and 100 m (H/W=2.0) (see Fig. 2 for a schematic overview).

For the radiation modelling, periodic boundaries are implicitly used at the domain sides, such that radiation can only be absorbed at the building surface or reflected towards the sky. The CFD model uses an inflow boundary condition with a prescribed uniform inlet velocity, outflow boundary condition with a zero diffusion flux for all variables, symmetry boundary condition at the top of the domain which does not allow a vertical velocity gradient and no-slip walls at the ground and building surfaces.

In addition to changes in building height, different components of the surface energy balance are switched on and off. Instead of performing a full factor separation analysis like Ryu and Baik [7] where all combinations of different processes were considered, the simplest case with only radiation is used as a starting point. From this basic case, complexity has been added by adding the conductive heat flux process with a zero-flux boundary condition (case 2) and sensible heat flux (case 3). The case including the sensible heat flux and fixed interior temperature is addressed separately.

Eight consecutive days were considered in the middle of June, which is the month where the sun is at its maximum zenith angle in the Netherlands. The simulated weather conditions correspond to sunny, cloud free weather. The maximum radiative components mentioned in Table 2 are a few tens of Wm^{-2} smaller than the maximum values observed in the Netherlands. By using eight days, quasi-steady state results are obtained that are independent on the initial conditions (the daily cycle is repetitive). For a point in the center of the canyon for $H/W=1.0$, differences between the last three days in the maximum surface temperature are below 1 °C, while the maximum conductive heat flux differs by 3 Wm^{-2}. The time step that is used is 6 min. The inlet air has a velocity of 4 ms^{-1} and a temperature of 20 °C and both are constant with height and time. The inlet wind speed of 4 ms^{-1} is used to avoid an urban heat island internal circulation that can develop in the presence of very weak background winds [43]. The wind speed of 4 ms^{-1} is similar to the study by Draxler [44], and leads to a wind speed above roof level of 2.5 ms^{-1}at the most downwind canyon, which is slightly lower than the 30 year average wind speed in the month June at weather station De Bilt in the Netherlands(www.klimaatatlas.nl).

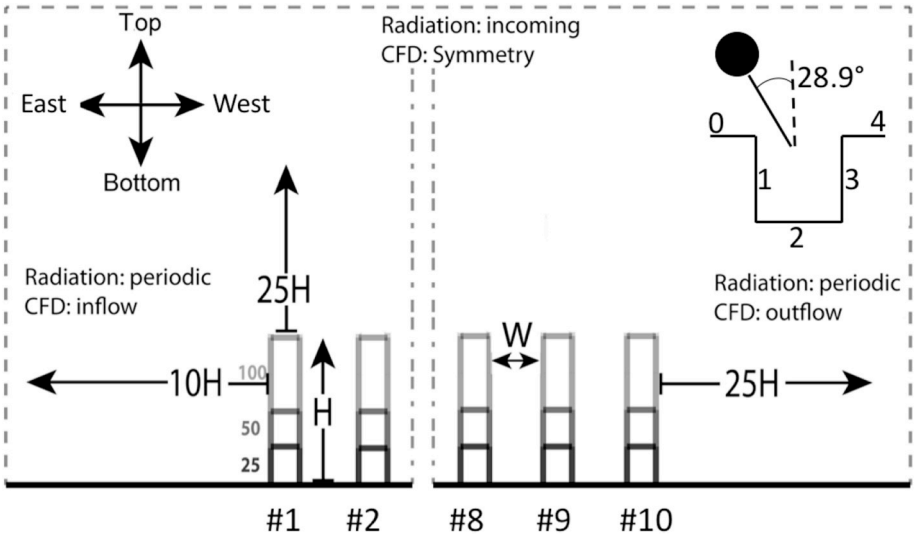

Figure 2. Schematic of the case set-up with changing H/W ratio. Ten buildings are spaced $W=50$ m apart, while building height (H) is varied. Plotting is done according to the inset in the top right, which also includes the solar position with zenith angle of 28.9°. Building orientation is shown in the top left, surface 1 is denoted as 'west-facing', surface 3 is denoted as 'east-facing'.

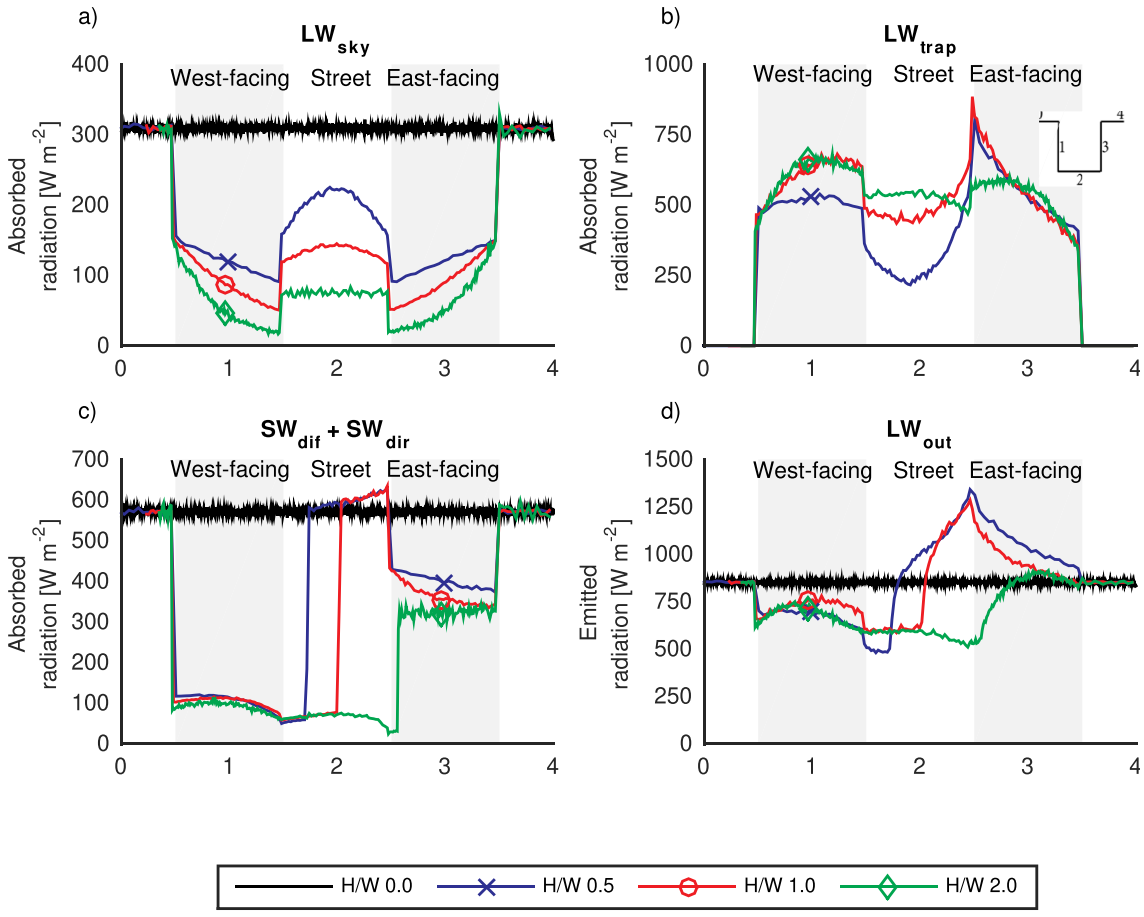

Fig. 3. Absorbed longwave radiation emitted by the sky, absorbed radiation due to longwave trapping, total absorbed shortwave radiation and emitted longwave radiation by walls in case of radiation only (case 1). Plotting follows the inset at the top right, except for a flat plate. Note the difference in scaling on the vertical axis for each plot.

Both for daytime and nighttime, constant values in time and height are used for the inlet wind speed and air temperature. The reason for using these strongly idealized lateral boundary conditions, that ignore the diurnal cycle of wind and temperature, is to increase the understanding of the individual processes such as the radiative forcing on the surface energy balance. By using more realistic, time-dependent input parameters, differentiating the different processes from the input parameters becomes much more difficult, which would limit the insights gained from this study. The initial surface temperature is set to 27 °C on all surfaces based on expected average surface temperatures over the complete canyon. In total, 8 diurnal cycles are simulated, such that the choice of the initial surface temperature does not influence the results. Other input parameters are shown in Table 2.

Fig. 2 illustrates how further results (Figs. 4–7) are plotted, where all vertical surfaces are scaled to a length of 1. This allows us to compare different H/W ratios in a single plot. For $H/W = 0$, the full domain is plotted (length of 1000 m) which is plotted as a scaled distance from 0 to 4.

3. Results

Even though multiple diurnal cycles were computed, the results presented here only show the results for the last computed day and the time instance where the sun reaches its highest position. The last day has been used, to ensure that the initial conditions do not have an influence on the results, and the diurnal cycle is repetitive. For details on the diurnal cycle of surface temperature, the conductive heat flux and sensible heat flux, please see Ref. [26]. The highest position of the sun is chosen, since radiation is strongest at this point in time, and will thus lead to the most clear relation between mean radiant temperature and surface temperature. Note that the sun is not directly overhead the canyon, such that there is shading of the west-facing wall.

3.1. Case with radiation only

The first case considers radiative equilibrium. Since there is no conduction or convection, this situation implies that all absorbed radiation should be emitted through longwave radiation. This case acts as the reference case, from which the effect of including additional process can be determined. Absorbed longwave radiation from the sky is shown in Fig. 3a, and is decreasing with increasing H/W ratio due to the reducing sky-view factor. For a flat terrain (H/W=0.0) fluctuations are seen in the absorbed radiation. This is due to the Monte-Carlo method, where a finite number of photons are emitted. As a result, each grid cell receives a slightly different amount of energy. The fluctuations are decreasing when more photons are emitted, but this comes at a cost of increasing computation time. These fluctuations are also seen when buildings are included.

Fig. 3b shows the absorbed longwave radiation that is emitted by the buildings and the ground surface. This longwave trapping effect shows an asymmetric pattern that is due to the differential solar radiative heating of the canyon surfaces. The sunlit surface is warmer, emits more radiation and therefore the longwave trapping effect in the corner between the street and sunlit wall is higher.

For $H/W = 0.5$ and $H/W = 1.0$, longwave trapping peaks at the corner between the ground and the east-facing wall. Trapping in the

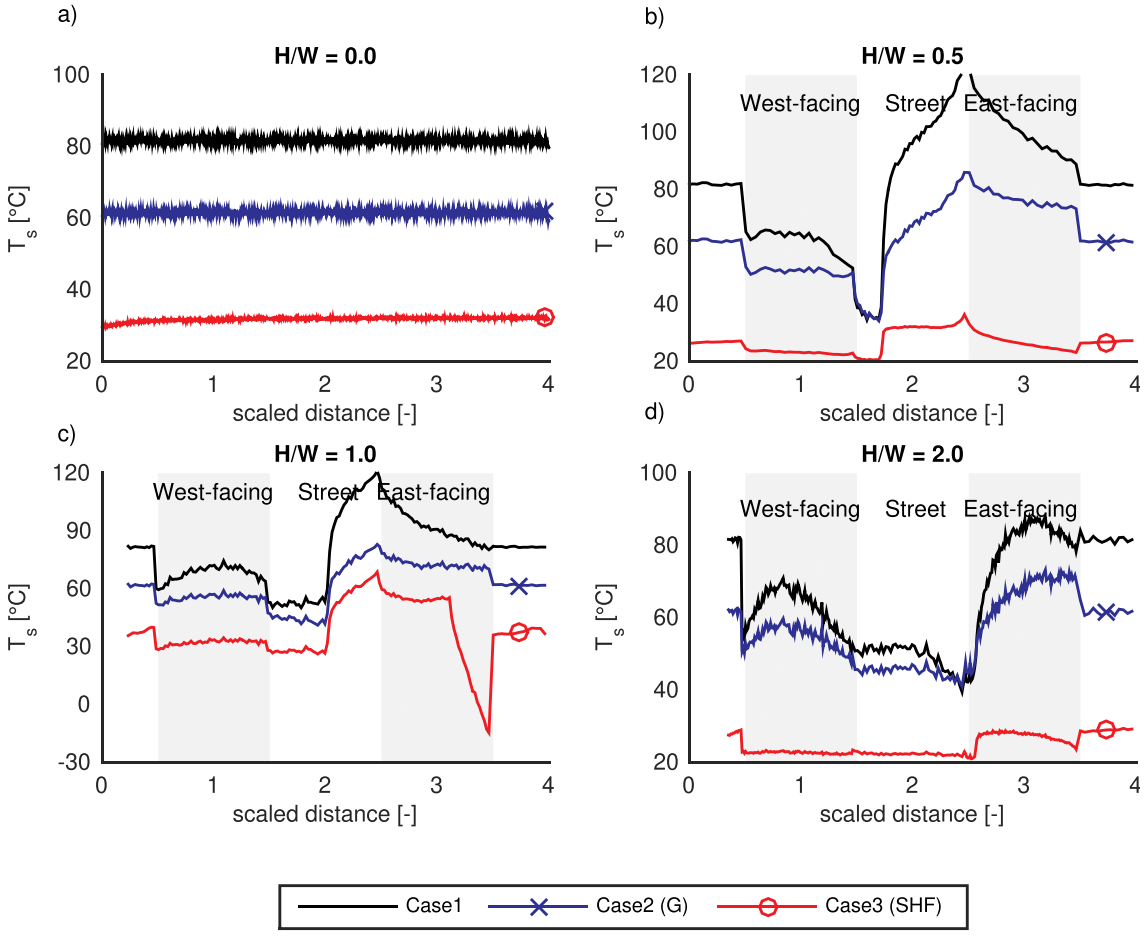

Fig. 4. Surface temperature for different H/W ratios (sub plots) and different cases (coloured lines). Different vertical scales are used in each plot to better visualize the temperature differences.

corner between the ground and the east-facing wall is higher compared to the corner with the west-facing wall, since surface temperature in the east-facing wall corner is higher, and thus there is more emitted longwave radiation. With increasing H/W ratio, there is less variation in the longwave trapping. With higher buildings, longwave radiation progresses towards two infinite plates that are facing each other, where there is a uniform distribution. The corners are of less importance for these larger H/W ratios.

The total absorbed shortwave radiation (direct and diffuse component) is shown in Fig. 3c. The trapping effect due to multiple reflections can be observed at the ground level, where the absorbed shortwave radiation exceeds that of the flat terrain for $H/W = 0.5$ and $H/W = 1.0$. The shadow location on the ground can also be observed, where $H/W = 1.0$ shows a larger shaded area of the ground surface as compared to $H/W = 0.5$. For $H/W = 2.0$, the street level is completely shaded.

Due to our assumption of radiation as the only transport means of heat, the total of all the absorbed radiative fluxes balances the emitted longwave radiation. This is shown in Fig. 3d, which displays a clear peak in emitted radiation for $H/W = 0.5$ and $H/W = 1.0$ at the lower corner between the ground and the east-facing wall, where emitted longwave radiation exceeds that of the flat plate. The longwave trapping effect and the absorbed shortwave radiation have approximately the same magnitude, while the magnitude of the absorbed longwave radiation emitted by the sky is much smaller. There is an imbalance over the canyon of 60 Wm^{-2}, which is due to the time stepping algorithm, where the emitted longwave radiation is based on the surface temperature computed in the previous time step. For $H/W = 2.0$, the lowest emitted radiation is in the corner between the street and the east-facing wall, at 500 Wm^{-2}, with the total absorbed radiation at roof level at 800 Wm^{-2}.

3.2. Surface temperature

From the radiation only case, more physical processes are added to study their effect on the surface temperature. For the radiation case, the surface temperature of a flat plate becomes very high at about 82 °C (see Fig. 4a). Note that this is not a prescribed surface temperature, but its high value follows directly from the balance between the absorbed and emitted radiation. These temperatures are in line with Garratt [45], who suggested that surface temperatures in the vicinity of 90–100 °C may occur for dry darkish soils of low thermal conductivity (0.1–0.2 $Wm^{-1}K^{-1}$), considering a simplified form of the surface energy balance equation, utilizing likely upper values of absorbed shortwave flux (1000 Wm^{-2}) and screen air temperature (55 °C).

If the conductive heat flux process is added, energy is transferred into the ground, reducing its surface temperature by 20 °C. The inclusion of the sensible heat flux allows for another energy transfer from the solid surface to air which even further reduces the surface temperature by 30 °C.

If obstacles are added, the effects of shadow casting (lower surface temperatures on the west-facing walls) and multiple shortwave reflections (higher surface temperature on the ground and the east-facing wall compared to the flat terrain) are clearly demonstrated for obstacles with $H/W = 0.5$ and $H/W = 1.0$ (Fig. 4b and c, respectively). The impact of multiple reflections is smaller for deeper canyons, where only a portion of the east-facing wall is directly illuminated. Surface temperatures at the ground level exceed these of the flat terrain, due to the

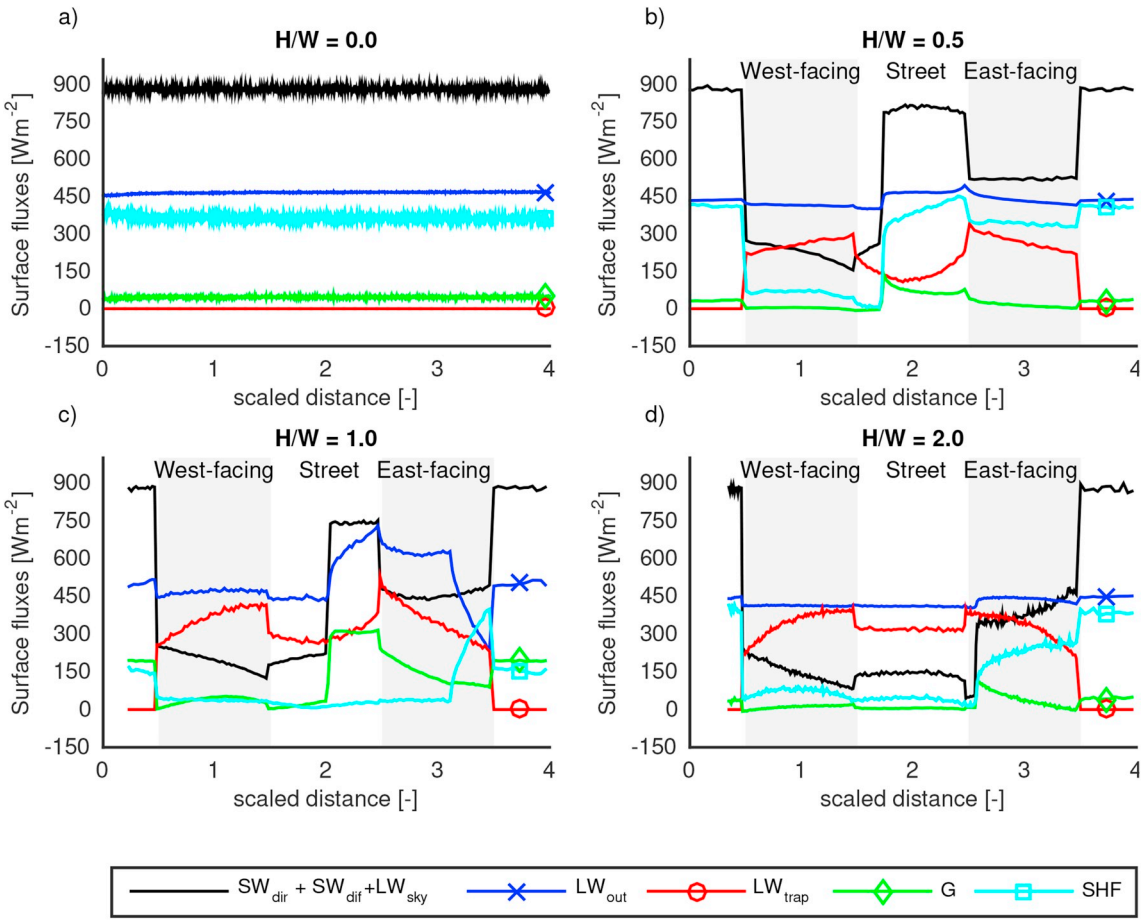

Fig. 5. Surface fluxes for different H/W ratios (sub plots) and physical processes (coloured lines) for case 3 (including conductive and sensible heat flux, but excluding latent heat flux). The same scale is used for all plots.

longwave trapping effect, which is 750 Wm^{-2} in the corner between the street and the east-facing wall. In the absence of conduction and sensible heat fluxes this additional radiative energy causes excessively high surface temperatures of about 120 °C.

The addition of the conductive heat flux influences the sunlit and shaded part of the canyon differently. In the shaded areas, the conductive heat flux has only a small effect. For $H/W = 2.0$, the conductive heat flux has the smallest influence. Note that a zero-flux boundary condition is used deep inside the obstacle and the ground, which impact will be discussed later.

The inclusion of the sensible heat flux filters out surface temperature differences for $H/W = 0.5$, where the temperature differs from 32 °C close to the east-facing wall to 20 °C at the corner between the west-facing wall and roof. For $H/W = 1.0$, the highest surface temperature is located in the corner between the east-facing wall and the ground. A sharp decrease in surface temperature is found at the top corner. This is due to a local very high turbulent viscosity (ν_t), which is directly influencing the sensible heat flux following from Equation (6). It is known that the standard $k-\varepsilon$ model computes too high values of turbulent kinetic energy at stagnation points [46]. The too large value of turbulent viscosity is directly increasing the sensible heat flux. The Durbin time-scale limiter τ may be applied, which bounds the turbulent viscosity and therefore also the turbulent heat flux [46]. Note that the same effect is also present for the other H/W ratios, but to a lesser extent. For $H/W = 2.0$, surface temperature is almost uniformly distributed, with temperature differences between 21 and 26 °C.

3.3. Surface fluxes

The surface temperature plots reveal, in a qualitative sense, which processes are more important. To get a more quantitative view, all individual fluxes are plotted in Fig. 5. In this plot, all absorbed radiation entering from the sky (SW_{dir}, SW_{dif} and LW_{sky}) is combined. Also note that positive values of LW_{out}, G and SHF indicate a cooling tendency of the surface.

For the flat plate (Fig. 5a) the absorbed radiation contributes 900 Wm^{-2} to the surface, while 450 Wm^{-2} is emitted through LW_{out}. The energy surplus is compensated by the sensible heat flux (375 Wm^{-2}) and the conductive heat flux (50 Wm^{-2}). At this moment in time, there is a flux imbalance of 25 Wm^{-2}.

When cases including obstacles are considered, absorbed radiation remains the largest contribution in the sunlit areas, although its relative contribution decreases for high H/W ratio, which was also shown in Fig. 3. The incoming shortwave radiation is divided over a larger surface area, which results in lower surface temperatures. The longwave trapping effect remains larger than the conductive or sensible heat flux. Compared to absorbed radiation from the sky, the longwave trapping is increasing for increasing H/W ratio.

The conductive heat flux shows very small contributions at the west-facing wall and the top part of the east-facing walls. Only at the location where the absorbed radiation peaks, the conductive heat flux is significantly transferring energy into the canyon material. The addition of the sensible heat flux shows a small cooling tendency of the west-facing walls. For $H/W = 0.5$, the sunlit parts of the street and the east-facing wall shows a much larger cooling effect, where energy is extracted

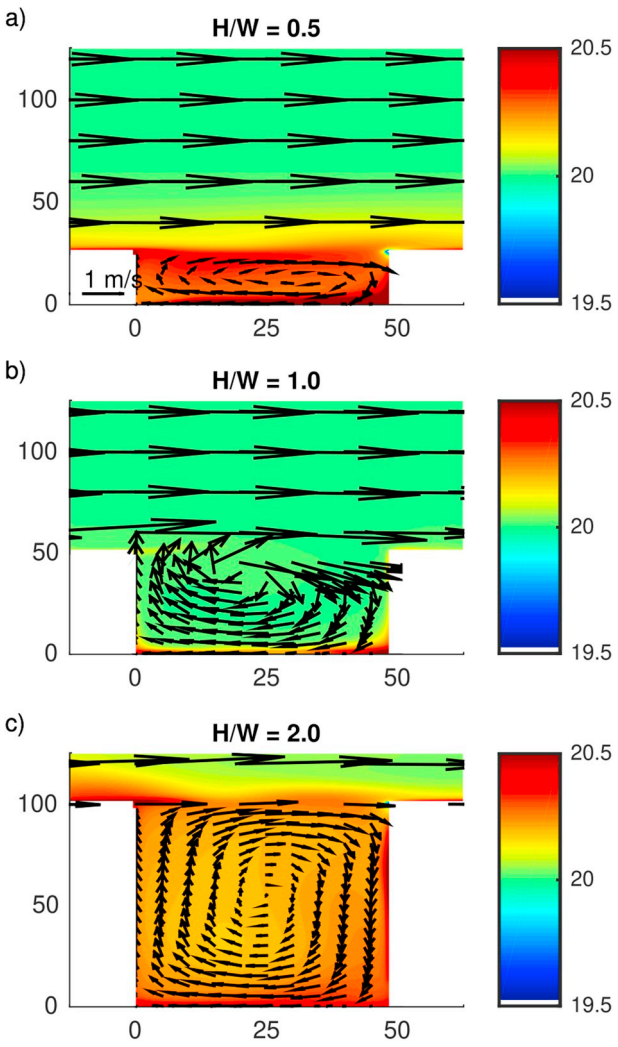

Fig. 6. Absolute air temperature (°C) and velocity vectors for Case 3 for different H/W ratios. The x-axis presents the distance from the west-facing wall in meters. Note the different length scales on the horizontal and vertical. A reference vector of $1 ms^{-1}$ is shown on the bottom left of panel a.

from the warmer surface. For $H/W = 1.0$ (Fig. 5c), the sensible heat flux at the ground surface is almost zero, which indicates that the temperature differences between the surface and the adjacent air are very small. The sharp peak in the sensible heat flux is clearly seen at the top corner between the roof and the east-facing wall, which is reducing the emitted longwave radiation directly. For $H/W = 2.0$, sensible heat flux increases from 5 Wm^{-2}at the ground level to 250 Wm^{-2}at the corner between the roof and the east-facing wall, and is generally larger than the conductive heat flux contribution.

3.4. Air temperature

Air temperature and velocity vectors for Case 3 are shown in Fig. 6. For $H/W = 0.5$, a warmer canyon is observed as compared to the free stream air temperature, and one single vortex is present. This is in contrast with results by Sini et al. [47], who found a second vortex in the lower left corner in the absence of buoyancy forces. The non-uniform heating of the canyon in the present study suppresses the formation of the second vortex. However, in our model simulations a small second vortex becomes present only if the buoyancy force is switched off. This result (not shown here) hints at a subtle effect of the non-uniform canyon heating on the suppression of the second vortex. From the east-facing wall, air is heated by the surface and forced towards the

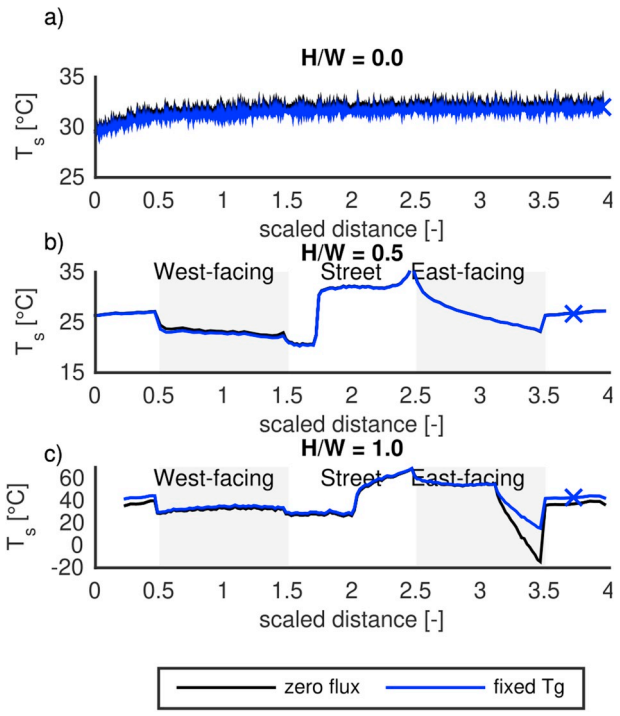

Fig. 7. Surface temperature for different H/W ratios (sub plots) for case 3 (including conductive and sensible heat flux, with a zero flux boundary condition) and the same case but with a fixed interior temperature T_g of 20 °C.

west-facing wall, where the highest air temperature is found. Air temperature inside the canyon is 1.5 °C higher than ambient air, which is comparable in magnitude to measurements from Giovannini et al. [48], who found temperature differences up to 2 °C for $H/W = 0.85$.

For $H/W = 1.0$ (Fig. 6b), a similar pattern of the flow structure is observed compared to $H/W = 0.5$, but with lower air temperatures. Air is locally heated close to the surfaces, with a slightly larger region in the corners where the wind speed is low. Warm air is transported from the west-facing wall upwards towards roof level, and from there dispersed to the centre of the canyon due to the free stream air flowing over the top. The temperature distribution within the canyon for $H/W = 1$ is remarkably different as compared to the other two examples shown for H/W equal to 0.5 and 2, respectively, in the sense that only a relatively small layer of warm air is found near the ground surface. For $H/W = 1$ the relatively warm air is more efficiently transported out of the canyon.

Similar to $H/W = 0.5$, a warmer canyon than the free stream air is seen for $H/W = 2.0$, with an average air temperature of 20.1 °C. Air temperature inside the canyon is rather uniformly distributed, with slightly higher temperatures along the east-facing wall. One single vortex is seen, but velocity inside the canyon is low. Other studies also presented a double vortex when one side of the canyon is heated, which is not observed here. These studies often apply uniform heating on one vertical wall, with typical temperature differences between two surfaces of 5 °C or 10 °C. In the present study, the application of an energy balance model at the solid surfaces lead to a non-trivial surface temperature distribution. Therefore, buoyancy forces are not constant inside the canyon, which can alter the formation of a double or single vortex structure. Further study is required to fully grasp the influence of these non-uniform temperature distributions and when the vortex structure changes inside the canyon. An extensive analysis of air flow in deep canyon (H/W=2.1) is provided in the study by Offerle et al. [49]. Measurements were conducted over a range of seasons and primarily analysed for sunny days. A distinction was made on warmer windward and leeward walls in combination with wind directions. When the leeward wall is heated, heat transfer is concentrated near the wall,

resulting in vertical transport of heat and less mixing. When this buoyant flow encounters the cross-canyon flow and the shear layer at the canyon top, the different flow layers become well mixed, such that this buoyant flow will be recirculated. Even though there is no cross flow in the present study, the mixing of the shear layer at the canyon top is also observed here. Note that the measurements by Offerle et al. [49] indicate a weaker influence of buoyancy effects compared to several reported numerical studies.

3.5. Influence of interior boundary condition

The zero-flux boundary condition implies that the interior temperature will be determined by the net radiation and the sensible heat flux. To investigate the impact of a zero-flux boundary condition on the results, we have performed a sequence of simulations for H/W up to 1.0 with another boundary condition in which a fixed interior temperature of 20 °C is prescribed.

The surface temperature is plotted in Fig. 7, and compares the Case 3 (including sensible heat flux, but with a zero-flux boundary condition) to the same case but with a fixed T_g. For $H/W = 0.0$, the difference between the two boundary conditions is about 1 °C, where the fixed T_g provides a lower surface temperature. For $H/W = 0.5$, there is only a small difference in the surface temperature of about 0.5 °C on the east-facing wall resulting from the use of the two different boundary conditions. For all other surfaces, there is no distinctive surface temperature difference when changing the interior boundary condition. For $H/W = 1.0$, the case with the fixed interior temperature provides a higher surface temperature, by 2 °C. Furthermore, the decrease in the surface temperature towards the top of the east-facing wall is smaller. The fixed interior temperature is able to extract more energy from the surface into the urban material, compared to the zero-flux boundary condition.

In general, the differences between the two boundary conditions (fixed interior temperature and zero flux) are small, provided that a reasonable estimate is given for the interior temperature. Fig. 8 compares the individual surface fluxes for $H/W = 1.0$. Differences are below 10 Wm^{-2} for the conductive heat flux, except for the corner between the east-facing wall and the roof.

Despite the small differences observed in the surface temperatures and fluxes in this study, the fixed interior temperature can act as an unlimited source of energy, forcing surface temperature towards the prescribed building interior temperature. The large impact of the indoor temperature on the outdoor environment has also been demonstrated by Theeuwes et al. [19] who studied the UHI with the WRF model, and showed a range of the UHI between 2 and 7 °C when changing building temperature from 5 to 23 °C.

The interior temperature boundary conditions therefore can be used as a 'tuning parameter' in which one can steer the model results by prescribing the desired ground temperature. For instance, when in the validation case the surface temperature is too low, one can prescribe a higher interior boundary temperature to 'solve' the problem. By using a zero-flux boundary condition, there is no user input, and the results cannot be controlled by the user to obtain the desired solution. Therefore, the choice was made to use the zero-flux boundary condition as the default option in this study.

3.6. Mean radiant temperature

The mean radiant temperature at a height of 2 m is shown in Fig. 9. For the flat plate (H/W=0.0), a mean radiant temperature of 69 °C is found. The threshold for moderate heat stress is at 55 °C, while strong heat stress is experienced above 60 °C [12,13], indicating that very strong heat stress is experienced. Inclusion of obstacles below $H/W = 1.0$ results in large spatial variations due to shading in this case. The mean radiant temperature in the sunlit part exceeds that of the flat terrain due to multiple reflections and longwave trapping and peaks at 90 °C for $H/W = 1.0$ (extreme heat stress), while a value of 45 °C is found in the shade (no thermal heat stress). For $H/W = 0.5$, a lower mean radiant temperature in comparison to $H/W = 1.0$ is found, but extreme heat stress is observed over a larger region due to a smaller shaded area. For $H/W = 2.0$, there is no sunlit part of the canyon at this

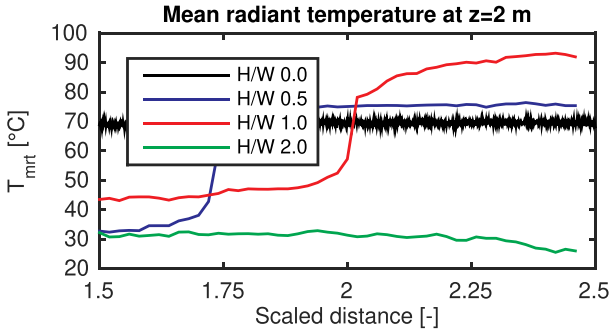

Fig. 9. Profiles of mean radiant temperature at z = 2 m height between buildings 8 and 9 for case 3.

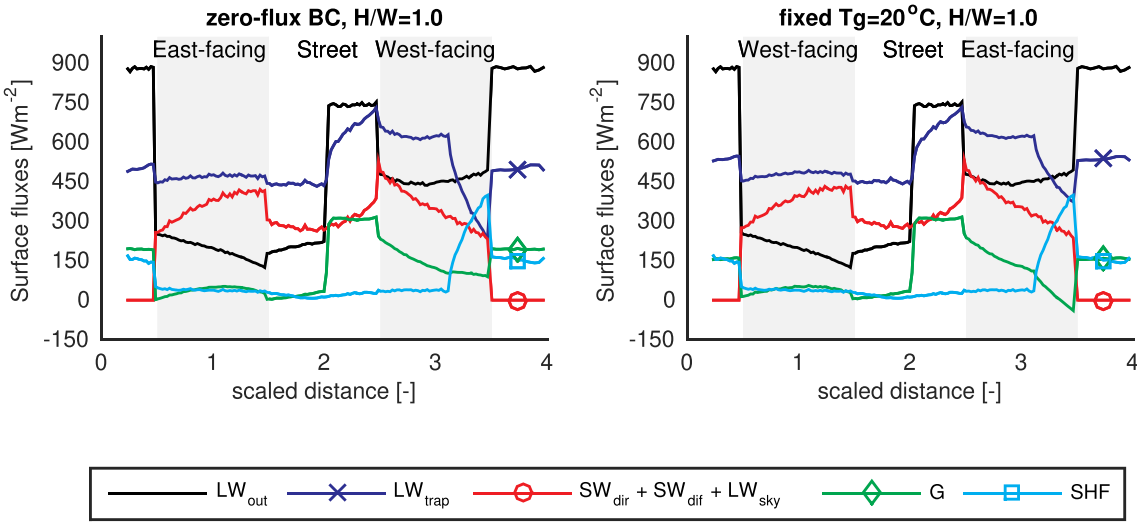

Fig. 8. Surface fluxes for $H/W = 1.0$ for case 3 (including conductive and sensible heat flux, with a zero flux boundary condition) and the same case but with a fixed interior temperature T_g of 20 °C.

height, and the mean radiant temperature is much more uniform and around 30 °C. The highest temperature is found near the west-facing wall, due to solar reflections from the east-facing wall.

For $H/W = 2.0$, a nearly constant surface temperature at the ground level is found. Surface temperatures for $H/W = 1.0$ are higher at the ground level compared to $H/W = 0.5$, especially in the sunlit area. The same is also seen in the mean radiant temperature. However, the mean radiant temperature is not only a function of surface temperature, but also of sky-based radiation (both shortwave and longwave). There is a thus a clear relation between the change in surface temperature and mean radiant temperature, although linking absolute temperatures show a less trivial relation.

4. Discussion

4.1. Results

Results in this study showed that for all H/W ratios the surface energy budget is strongly controlled by radiative terms. With increasing H/W ratio, the longwave trapping effect and conductive heat flux become relatively more important. This is similar to the findings by Marciotto et al. [17], who found the largest contribution from the net radiation (all absorbed and emitted radiative terms combined) for $H/W = 0.5$, while for $H/W = 10.0$ the conductive energy flux becomes almost equally important compared to the net radiation.

Mean radiant temperature showed large spatial changes due to shadow locations, where mean radiant temperature is up to 10 °C higher compared to air temperature in shaded areas and up to 70 °C higher in sunlit areas. Similar results were found by Ali-Toudert and Mayer [50], although the mean radiant temperature in the sunlit part in their study is about 10 °C lower than in our study.

The large impact of radiation on the urban energy budget, in particular for low H/W ratios, allows for a relatively simple link between mean radiant temperature and the surface temperature. The strong relation between surface temperature and mean radiant temperature is exploited in the modelling approach followed by simulation models Solweig [11] and RayMan [20], in which the computation of the surface temperature is parametrized but accurate results are obtained for mean radiant temperatures. This study indicates that for $H/W = 2.0$, the sensible heat transfer becomes more important compared to the conductive heat flux, which is highly parametrized in both Solweig and RayMan. This might compromise the accuracy of these models for deep canyons.

The addition of a CFD model in URBSIM gives insight in the impact of surface temperature on the air temperature. There is a complex interplay between forced convection (free stream air) and natural convection. Different vortex dynamics inside a canyon as a function of surface temperature have also been found by Magnusson et al. [51] who found two vortices for a canyon with $H/W = 2.5$. When the leeward wall of the canyon was heated, the weak lower vortex disappeared and one vortex remained. However, these simulations where conducted with a fixed surface temperature, without feedback from warmer/colder air on the surface.

4.2. Model deficiencies

URBSIM has been developed with the goal to reduce the amount of assumptions that are made for modelling the urban micro-scale. Therefore, a Monte-Carlo radiation model and CFD model were used, which represent the physical processes as detailed as possible. The model results show a small increase in the air temperature inside the canyon for $H/W = 0.5$ and $H/W = 2.0$ as compared to the ambient temperature above roof level. These results appear physically sound. However, a weakness of the model is the representation of the dynamics near roof corners, where the CFD model produces a too large value for the turbulent viscosity [46], which in turn directly affects the turbulent heat flux and reduces the surface temperature locally.

In order to take all processes into account in such high detail, the urban geometry is highly simplified by only taking into account a 2D street canyon. Taking into account a full 3D urban geometry would be computationally too expensive. Within URBSIM, it is assumed that if building arrays are much longer than their height, they can be considered to be 2D. Santamouris et al. [52], Coronel and lvarez [53] and Giovannini et al. [48] performed measurements in canyons with ratios L/H of the building length L to the height H in the range between 1.25 and 5.5, and found significant 3D effects on the air flow. All of these measurements observed that flow characteristics inside the canyon are either due to circulatory vortices or finite canyon length effects that are related to 3D flow patterns. These findings indicate that even with very long canyons, 3D effects are present, which are absent in the 2D model used in this study.

In addition to the 2D assumption, there is the effect of temporal variations. Although the whole diurnal cycle is computed, the current paper only focussed on the situation at one time instance. Especially the conductive heat flux shows large diurnal variations. Results shown here are therefore always a function of the situation of the previous time-steps. The large diurnal variations have been reduced in this paper by considering highly idealized conditions, such as a symmetrical 2D street canyon, constant inlet wind speed and air temperature, and a fully developed flow in the canyon of consideration.

Despite these assumptions, calculations are expensive and require substantial amounts of computation time. Similar observation was made by Robitu et al. [25]. Therefore, the step to a 3D URBSIM program is not yet possible, and model simplifications must be made. The two most expensive computations are the sensible heat flux (CFD model) and the radiation (Monte-Carlo method). For the sensible heat flux computation, no suitable alternatives are present at the moment, that compute the airflow inside the canyon and handle the complex balance between forced convection and buoyancy forces. For the radiation model, a simpler model is available using view factor algebra. Especially for these simple urban canyon configurations, computation times for the radiative components using the view factor approach should be small, providing very similar results to the Monte-Carlo method. One limitation using view factor algebra is that only a limited number of reflections are typically taken into account (one or two reflections). Therefore, the radiation scheme is the most likely candidate to reduce the computation time, without deteriorating the results.

One process that has not been investigated in this study is the latent heat flux, which is extracting energy from the urban canyon through evaporation of water. Taking into account the latent heat flux requires one additional parameter in the CFD model (humidity) and a water balance on the building surfaces. As Theeuwes et al. [54] demonstrated with the aid of a diagnostic equation, the inclusion of the vegetation fraction (directly relating to the latent heat flux) is required to accurately compute the city-scale UHI effect.

5. Conclusions

This study focussed on the daytime micro-climatic conditions inside an idealized 2D canyon. A building-resolving simulation model has been used, which includes key physical processes like radiation, conduction and ventilation by air flow at a 1 m spatial resolution. A range of canyon height to width (H/W) ratios and physical processes are considered.

Results showed that the daytime energy budget is strongly controlled by radiation, where absorbed radiation from the sky (SW_{dir}, SW_{dif} and LW_{sky}, including their multiple reflections) is the main source of energy at the surface, followed by trapped longwave radiation (energy emitted from the surface and absorbed at another location). The radiative components are, however, decreasing with increasing building height, while the conductive heat flux is increasing. Mean radiant temperature increased locally for $H/W = 0.5$ and $H/W = 1.0$ compared to a flat plate.

This is due to increased multiple reflections of shortwave radiation and longwave trapping. For deeper canyons, there is no direct sunlight reaching the street level, and mean radiant temperature drops quickly.

The link between surface temperature and mean radiant temperature can be made (at least from a quantitative point of view) relatively easy, since both are largely dependent on radiative fluxes. This relation allows for simplified models, where the computation of the surface temperature is parametrized but accurate results are obtained for mean radiant temperatures [11,20]. The link between surface and air temperature is much harder to make. Air temperature inside the canyon is determined by a complex competition between forced convection (which is a function of free stream wind speed) and natural convection (buoyancy forces). This makes it difficult to develop a parametrization that holds for all H/W ratios and on every individual canyon surface.

The model used in the present study takes all processes into account in high detail, where the input of the user has been minimised as much as possible. The down-side of this approach is that calculations are costly and time-consuming, and the same approach can't be extended to 3D environments due to the large computational requirements of the CFD model and the Monte-Carlo model, in which the number of emitted photons would increase drastically. For these simple building shapes, the Monte-Carlo model may be replaced by a much faster view-factor model.

Furthermore, coupling to a large scale model, such as presented in the overview paper by Chen et al. [55] could be pursued to allow for more detailed meteorological input conditions. Instead of using constant parameters as done now, a diurnal cycle in air temperature and wind speed could be used.

Acknowledgment

This study is funded by the Dutch Climate Proof Cities consortium [56], which is part of the Knowledge For Climate program (http://knowledgeforclimate.climateresearchnetherlands.nl/climateproofcities).

References

[1] T.R. Oke, Canyon geometry and the nocturnal urban heat island: comparison of scale model and field observations, J. Climatol. 1 (1981) 237–254.
[2] K. Klysik, K. Fortuniak, Temporal and spatial characteristics of the urban heat island of Lodz, Poland, Atmos. Environ. 33 (1999) 3885–3895.
[3] Y.-H. Kim, J.-J. Baik, Daily maximum urban heat island intensity in large cities of Korea, Theor. Appl. Climatol. 79 (2004) 151–164.
[4] C.S.B. Grimmond, Urbanization and global environmental change: local effects of urban warming, Geogr. J. 173 (2007) 83–88.
[5] G.J. Steeneveld, S. Koopmans, B.G. Heusinkveld, L.W.A. van Hove, A.A. M. Holtslag, Quantifying urban heat island effects and human comfort for cities of variable size and urban morphology in The Netherlands, J Geophys Res Atmos 116 (2011).
[6] H. Taha, Urban climates and heat islands: albedo, evapotranspiration, and anthropogenic heat, Energy Build. 25 (1997) 99–103.
[7] Y.-H. Ryu, J.-J. Baik, Quantitative analysis of factors contributing to urban heat island intensity, J Appl Meteorol Climatol 51 (2012) 842–854.
[8] A. Soltani, E. Sharifi, Daily variation of urban heat island effect and its correlations to urban greenery: a case study of Adelaide, Front. Archi. Res. 6 (2017) 529–538.
[9] P. Höppe, The physiological equivalent temperature: a universal index for the biometeorological assessment of the thermal environment, Int. J. Biometeorol. 43 (1999) 71–75.
[10] D. Fiala, G. Havenith, P. Bröde, B. Kampmann, G. Jendritzky, UTCI-Fiala multi-node model of human heat transfer and temperature regulation, Int. J. Biometeorol. 56 (2012) 429–441.
[11] F. Lindberg, B. Holmer, S. Thorsson, Solweig 1.0 – modelling spatial variations of 3D radiant fluxes and mean radiant temperature in complex urban settings, Int. J. Biometeorol. 52 (2008) 697–713.
[12] A. Monteiro, V. Carvalho, C. Sousa, Excess mortality and morbidity during July 2006 heat wave in Porto, Portugal - T_{mrt} efficiency to anticipate negative effects on health, in: Proceedings of the 8th International Conference on Urban Climates, Dublin, Ireland, 6–10 August, 2012.
[13] S. Thorsson, J. Rocklov, J. Konarska, F. Lindberg, B. Holmer, B. Dousset, D. Rayner, Mean radiant temperature – a predictor of heat related mortality, Urban Clim 10 (Part 2) (2014) 332–345. ICUC8: The 8th International Conference on Urban Climate and the 10th Symposium on the Urban Environment.
[14] J. Barlow, Progress in observing and modelling the urban boundary layer, Urban Clim 10 (Part 2) (2014) 216–240. ICUC8: The 8th International Conference on Urban Climate and the 10th Symposium on the Urban Environment.
[15] H. Kusaka, H. Kondo, Y. Kikegawa, F. Kimura, A simple single-layer urban canopy model for atmospheric models: comparison with multi-layer and slab models, Bound-Lay Meteorol 101 (2001) 329–358.
[16] T.R. Oke, Street design and urban canopy layer climate, Energy Build. 11 (1988) 103–113.
[17] E.R. Marciotto, A.P. Oliveira, S.R. Hanna, Modeling study of the aspect ratio influence on urban canopy energy fluxes with a modified wall-canyon energy budget scheme, Build. Environ. 45 (2010) 2497–2505.
[18] V. Masson, A physically-based scheme for the urban energy budget in atmospheric models, Bound-Lay Meteorol 94 (2000) 357–397.
[19] N.E. Theeuwes, G.J. Steeneveld, R.J. Ronda, B.G. Heusinkveld, L.W.A. van Hove, A. A.M. Holtslag, Seasonal dependence of the urban heat island on the street canyon aspect ratio, Q J Roy Meteorol Soc 140 (2014) 2197–2210.
[20] A. Matzarakis, Estimation and Calculation of the Mean Radiant Temperature within the Urban Structure. Manual to RayMan, University of Freiburg, Germany, 2000.
[21] E. Krayenhoff, J. Voogt, A microscale three-dimensional urban energy balance model for studying surface temperatures, Bound-Lay Meteorol 123 (2007) 433–461.
[22] M. Bruse, Entwicklung des prognostischen numerischen Modells ENVI-met zur Simulation der Wind-, Temperatur- und Feuchteverteilung in Staddtischen Strukturen, Ph.D. thesis, University of Bochum, 1999.
[23] D. Hertel, U. Schlink, How to convert urban energy balance into contributions to urban excess temperatures? Methods 6 (2019) 132–142.
[24] Y. Toparlar, B. Blocken, B. Maiheu, G. van Heijst, A review on the cfd analysis of urban microclimate, Renew. Sustain. Energy Rev. 80 (2017) 1613–1640.
[25] M. Robitu, M. Musy, C. Inard, D. Groleau, Modeling the influence of vegetation and water pond on urban microclimate, Sol. Energy 80 (2006) 435–447.
[26] P.J.C. Schrijvers, H.J.J. Jonker, S. Kenjeres, S.R. de Roode, Breakdown of the night time urban heat island energy budget, Build. Environ. 83 (2015) 50–64 (Special Issue: Climate adaptation in cities).
[27] P.J.C. Schrijvers, H.J.J. Jonker, S. Kenjeres, S.R. de Roode, The effect of using a high-albedo material on the Universal Temperature Climate Index within a street canyon, Urban Climate 17 (2016) 284–303.
[28] A. Skartveit, J.A. Olseth, M.E. Tuft, An hourly diffuse fraction model with correction for variability and surface albedo, Sol. Energy 63 (1998) 173–183.
[29] S. Thorsson, F. Lindberg, I. Eliasson, B. Holmer, Different methods for estimating the mean radiant temperature in an outdoor urban setting, Int. J. Climatol. 27 (2007) 1983–1993.
[30] S. Madronich, Photodissociation in the atmosphere: 1. Actinic flux and the effects of ground reflections and clouds, J Geophys Res Atmos 92 (1987) 9740–9752.
[31] S. Kenjeres, K. Hanjalic, Transient analysis of Rayleigh-Benard convection with a RANS model, Int. J. Heat Fluid Flow 20 (1999) 329–340.
[32] S. Kenjeres, K. Hanjalic, LES, T-RANS and hybrid simulations of thermal convection at high Ra numbers, Int. J. Heat Fluid Flow 27 (2006) 800–810.
[33] S. Kenjeres, K. Hanjalic, Tackling complex turbulent flows with transient RANS, Fluid Dyn. Res. 41 (2009) 1–32.
[34] S. Kenjeres, B. ter Kuile, Modelling and simulations of turbulent flows in urban areas with vegetation, J. Wind Eng. Ind. Aerodyn. 123 (Part A) (2013) 43–55.
[35] S. Kenjeres, S. de Wildt, T. Busking, Capturing transient effects in turbulent flows over complex urban areas with passive pollutants, Int. J. Heat Fluid Flow 51 (2015) 120–137.
[36] B. Launder, D. Spalding, The numerical computation of turbulent flows, Comput. Methods Appl. Math. 3 (1974) 269–289.
[37] H. Versteeg, W. Malalasekera, An Introduction to Computational Fluid Dynamics, Pearson Education Limited, Harlow, 1995.
[38] J. Santiago, A. Martilli, F. Martin, CFD simulation of airflow over a regular array of cubes. Part I: three-dimensional simulation of the flow and validation with wind-tunnel measurements, Bound-Lay Meteorol 122 (2007) 609–634.
[39] A.A. Grachev, E.L. Andreas, C.W. Fairall, P.S. Guest, P.O.G. Persson, On the turbulent Prandtl number in the stable atmospheric boundary layer, Bound-Lay Meteorol 125 (2007) 329–341.
[40] D. Li, Turbulent Prandtl number in the atmospheric boundary layer - where are we now? Atmos. Res. 216 (2019) 86–105.
[41] S.R. de Roode, H.J.J. Jonker, B.J.H. van de Wiel, V. Vertregt, V. Perrin, A diagnosis of excessive mixing in smagorinsky subfilter-scale turbulent kinetic energy models, J. Atmos. Sci. 74 (2017) 1495–1511.
[42] R.A. Memon, D.Y. Leung, C.-H. Liu, Effects of building aspect ratio and wind speed on air temperatures in urban-like street canyons, Build. Environ. 45 (2010) 176–188 (International Symposium on the Interaction between Human and Building Environment Special Issue Section).
[43] T. Oke, The Heat Island of the Urban Boundary Layer: Characteristics, Causes and Effects vol. 277, NATO ASI Series e Applied Sciences-Advanced Study Institute, 1995, pp. 81–108.
[44] R.R. Draxler, Simulated and observed influence of the nocturnal urban heat island on the local wind field, J. Appl. Meteorol. Climatol. 25 (1986) 1125–1133.
[45] J. Garratt, The Atmospheric Boundary Layer, Cambridge University Press, 1992.
[46] P.A. Durbin, On the k-ε stagnation point anomaly, Int. J. Heat Fluid Flow 17 (1996) 89–90.
[47] J.-F. Sini, S. Anquetin, P.G. Mestayer, Pollutant dispersion and thermal effects in urban street canyons, Atmos. Environ. 30 (1996) 2659–2677.

[48] L. Giovannini, D. Zardi, M. de Franceschi, Characterization of the thermal structure inside an urban canyon: field measurements and validation of a simple model, J. Appl. Meteorol. Climatol. 52 (2013) 64–81.
[49] B. Offerle, I. Eliasson, C.S.B. Grimmond, B. Holmer, Surface heating in relation to air temperature, wind and turbulence in an urban street canyon, Bound-Lay Meteorol. 122 (2007) 273–292.
[50] F. Ali-Toudert, H. Mayer, Numerical study on the effects of aspect ratio and orientation of an urban street canyon on outdoor thermal comfort in hot and dry climate, Build. Environ. 41 (2006) 94–108.
[51] S. Magnusson, A. Dallman, D. Entekhabi, R. Britter, H. Fernando, L. Norford, On thermally forced flows in urban street canyons, Environ. Fluid Mech. 14 (2014) 1–15.
[52] M. Santamouris, N. Papanikolaou, I. Koronakis, I. Livada, D. Asimakopoulos, Thermal and air flow characteristics in a deep pedestrian canyon under hot weather conditions, Atmos. Environ. 33 (1999) 4503–4521.
[53] J. Coronel, S. Álvarez, Experimental work and analysis of confined urban spaces, Sol. Energy 70 (2001) 263–273.
[54] N.E. Theeuwes, G.-J. Steeneveld, R.J. Ronda, A.A.M. Holtslag, A diagnostic equation for the daily maximum urban heat island effect for cities in northwestern europe, Int. J. Climatol. 47 (2017) 443–454.
[55] F. Chen, H. Kusaka, R. Bornstein, J. Ching, C.S.B. Grimmond, S. Grossman-Clarke, T. Loridan, K.W. Manning, A. Martilli, S. Miao, D. Sailor, F.P. Salamanca, H. Taha, M. Tewari, X. Wang, A.A. Wyszogrodzki, C. Zhang, The integrated wrf/urban modelling system: development, evaluation, and applications to urban environmental problems, Int. J. Climatol. 31 (2011) 273–288.
[56] R.A.W. Albers, P. Bosch, B. Blocken, A.V.D. Dobbelsteen, L.V. Hove, T. Spit, Overview of challenges and achievements in the climate Proof cities program, Build. Environ. 83 (2015) 1–10 (Special Issue: Climate adaptation in cities).